Inorganic Chemistry
Article
pubs.acs.org/IC

Structure–Activity Relationships in Cytotoxic Au^I/Au^{III} Complexes Derived from 2-(2′-Pyridyl)benzimidazole

Laura Maiore,[†] Maria Carla Aragoni,[†] Carlo Deiana,[†] Maria Agostina Cinellu,[‡] Francesco Isaia,[†] Vito Lippolis,[†] Anna Pintus,[†] Maria Serratrice,[‡] and Massimiliano Arca*[,†]

[†]Dipartimento di Scienze Chimiche e Geologiche, Università degli Studi di Cagliari, S.S. 554 bivio per Sestu, 09042 Monserrato (Cagliari), Italy

[‡]Dipartimento di Chimica e Farmacia, Università degli Studi di Sassari, Via Vienna 2, 07100 Sassari, Italy

Supporting Information

ABSTRACT: Gold(I) and gold(III) complexes derived from 2-(2′-pyridyl)-benzimidazole (pbiH) were proven to be a promising class of in vitro antitumor agents against A2780 human ovarian cancer cells. In this paper, a comparative electrochemical, UV–vis absorption, and emission spectroscopic investigation is reported on pbiH, the two mononuclear Au^{III} complexes $[(pbi)AuX_2]$ (X = Cl (**1**), AcO (**2**)), the four mononuclear Au^I derivatives [(pbiH)AuCl] (**3**), $[(pbiH)Au(PPh_3)]PF_6$ ((**4**$^+$)(PF_6^-)), $[(pbi)Au(PPh_3)]$ (**5**), and [(pbi)Au(TPA)] (**6**), the three mixed-valence Au^{III}/Au^I complexes $[(\mu\text{-pbi})Au_2Cl_3]$ (**7**), $[(Ph_3P)Au(\mu\text{-pbi})AuX_2]PF_6$ (X = Cl ((**8**$^+$)(PF_6^-)), AcO ((**9**$^+$)(PF_6^-))), and the binuclear Au^I–Au^I compound $[(\mu\text{-pbi})Au_2(PPh_3)_2]PF_6$ ((**10**$^+$)(PF_6^-)). All complexes feature irreversible reduction processes related to the Au^{III}/Au^I or Au^I/Au^0 processes and peculiar luminescent emission at about 360–370 nm in CH_2Cl_2, with quantum yields that are remarkably lower ($(0.7–14.5) \times 10^{-2}$) in comparison to that determined for the free pbiH ligand (31.5×10^{-2}) in the same solvent. The spectroscopic and electrochemical properties of all complexes were interpreted on the grounds of time-dependent PBE0/DFT calculations carried out both in the gas phase and in CH_2Cl_2 implicitly considered within the IEF-PCM SCRF approach. The electronic structure of the complexes, and in particular the energy and composition of the Kohn–Sham LUMOs, can be related to the antiproliferative properties against the A2780 ovarian carcinoma cell line, providing sound quantitative structure–activity relationships and shedding a light on the role played by the global charge and nature of ancillary ligands in the effectiveness of Au-based antitumor drugs.

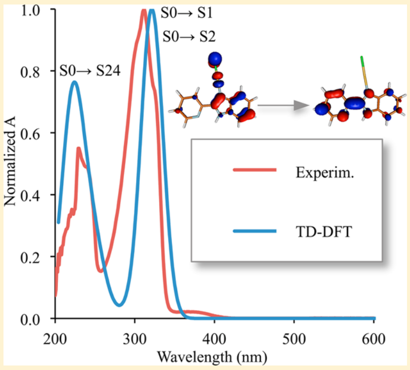

■ INTRODUCTION

The wide clinical success of platinum compounds in the medical treatments of cancer has prompted an increasing interest toward other platinum and nonplatinum metallodrugs that might exhibit comparable cytotoxic properties, hopefully accompanied by a different pattern of antitumor specificities and by a more favorable toxicological and/or pharmacological profile. During the past three decades, several new classes of metal compounds were intensely investigated as possible anticancer agents based on a variety of metals,[1] including ruthenium,[2] tin,[3] gallium,[3] titanium,[3] palladium,[4] gold,[5] copper,[6] and a few others.[7] Among these, gold compounds are some of the most promising candidates in antitumor drug development, and many examples of both gold(I) complexes with various phosphinic,[8] thiolato[9] and carbenic N-heterocyclic ligands[10] and gold(III) complexes with several polyamines,[11] polypyridines,[12] porphyrins,[13] and dithiocarbamato ligands[14] and cyclometalated compounds[15] have been reported in the literature with very favorable antiproliferative effects in vitro and in vivo. Recent studies attested to the fact that these kinds of derivatives display high activities against a series of cancer cell lines, embracing those resistant to common platinum-based chemotherapics, sometimes accompanied by a relevant pattern of selectivity, probably due to a different mechanism of action. Although gold(III) is isoelectronic and isostructural with platinum(II), it has been found that the interaction with DNA of most of the cytotoxic gold(III) compounds is electrostatic in nature and reversible and only a few exceptions were reported,[16] thus suggesting a mechanism of cytotoxicity different from that of cisplatin. Notably, strong inhibition of specific enzymatic targets, such as thioredoxin reductase, glutathione reductase, and peroxidase, and associated deregulation of mitochondrial functions and consequent proapoptotic effects were clearly documented in selected cases.[16] Other studies, also carried out in vivo, have shown that also the proteasome could be a primary target of gold complexes.[17] Furthermore, a number of gold complexes displayed potential pharmacological properties also against different diseases[18] such as parasitic disease (malaria,[19] leishmania,[20] and trypanosomiasys[21]), viral infections (HIV-1),[22] asthma,[23] and recently also against prions.[24] During the past decade some of the authors reported a series of gold(III) dinuclear oxo-bridged compounds bearing α-diiminic ligands (variously substituted

Received: January 4, 2014
Published: March 28, 2014

dx.doi.org/10.1021/ic500022a | *Inorg. Chem.* 2014, 53, 4068–4080

2,2′-bipyridine and 1,10-phenanthroline derivatives) with very potent cytotoxic properties against a number of human tumor cell lines.[25] Initial correlations between structure and activity were also evaluated on this class of compounds, suggesting that, within a given series, the oxidizing power affects the antitumor activity.[26] Therefore, analysis of the electrochemical behavior and the electronic−structural characterization could be, hopefully, a valid support to better understand the redox processes involved in the transformations of the original species and the mechanism of action of gold cytotoxic compounds.

Recently, some of the authors reported on the synthesis and characterization of a series of novel mono- and binuclear gold complexes bearing a 2-(2′-pyridyl)benzimidazole ligand (pbiH).[27] This is a very versatile multidonor ligand displaying three potential donor atoms, one sp^3- and two sp^2-hybridized N-donors, and is particularly interesting in view of its own pharmacological properties as an antibacterial[28] and anti-inflammatory agent.[29] The series of pbi-based investigated complexes (Chart 1) includes the two mononuclear Au^{III} compounds [(pbi)AuX$_2$] (X = Cl (**1**), AcO (**2**)), four mononuclear Au^{I} derivatives bearing chloride ([(pbiH)AuCl] (**3**)) or phosphines as ancillary ligands ([(pbiH)Au(PPh$_3$)]PF$_6$ ((**4**$^+$)(PF$_6^-$)) and [(pbi)AuL] (L = PPh$_3$ (**5**), 1,3,5-triaza-7-phosphaadamantane (TPA) (**6**)), three novel mixed-valence Au^{III}−Au^{I} complexes of the type [(μ-pbi)Au$_2$Cl$_3$] (**7**) and [(Ph$_3$P)Au(μ-pbi)AuX$_2$]PF$_6$ (X = Cl ((**8**$^+$)(PF$_6^-$)), AcO ((**9**$^+$)(PF$_6^-$))), and the binuclear Au^{I}−Au^{I} compound [(μ-pbi)Au$_2$(PPh$_3$)$_2$]PF$_6$ ((**10**$^+$)(PF$_6^-$)). In complexes **3** and **4**$^+$ the ligand coordinates the metal center in its neutral form, pbiH, while the remaining complexes feature the ligand in its deprotonated form, pbi$^-$.[27]

Chart 1. Atom-Labeling Scheme of pbiH and the Gold Complexes 1−3, 4$^+$, 5−7, and 8$^+$−10$^+$ ^{a}s

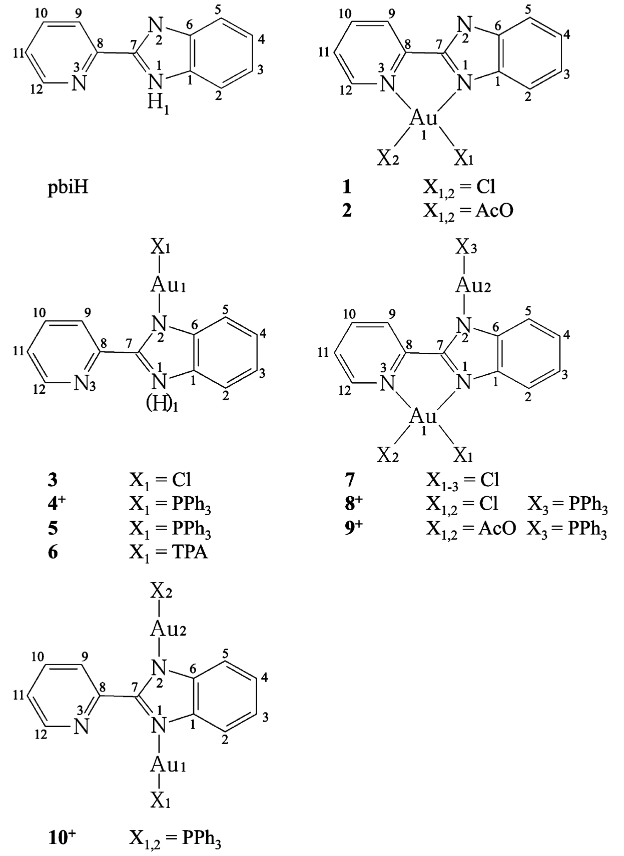

^{a}The atom N1 is protonated in complexes **3** and **4**$^+$. All cationic complexes were prepared as PF$_6^-$ salts.

All compounds were characterized, and the crystal structures of compounds **6**, **7**, and (**10**$^+$)(PF$_6^-$) were reported.[27] The stability of complexes **1**−**3**, **4**$^+$, **5**−**7**, and **8**$^+$−**10**$^+$ under physiological-like conditions was evaluated spectroscopically, and all compounds were quite stable even in the presence of 10 equiv of sodium ascorbate as reducing agent.[27] Some of these complexes displayed high cytotoxicity in vitro against human ovarian carcinoma cell lines both sensitive (A2780/S) and resistant (A2780/R) to cisplatin.[27,30]

With the aim of developing relationships capable of understanding and possibly predicting the structural features determining the antiproliferative activity of gold complexes deriving from the pbiH ligand, an insight into the electronic structure of the complexes **1**−**10**$^+$ is presented here, based on electrochemical, UV−vis spectroscopic and fluorimetric measurements, supported by theoretical calculations carried out at Density Functional Theory (DFT) level.

■ RESULTS AND DISCUSSION

The ligand pbiH was synthesized according to literature methods[31] through condensation of picolinic acid and 1,2-phenylendiamine in polyphosphoric acid at 180 °C. The synthesis of the complexes **1**−**3**, **4**$^+$, **5**−**7**, and **8**$^+$−**10**$^+$ has been discussed previously in detail.[27] Gold(III) adducts **1** and **2** were obtained by the reaction of pbiH with an equimolar amount of NaAuCl$_4$ in aqueous media and Au(AcO)$_3$ in a refluxed AcOH solution, respectively. Gold(I) derivatives **3** and (**4**$^+$)(PF$_6^-$), which bear the ligand in its neutral form, were prepared by reacting pbiH with [(THT)AuCl] and [(Ph$_3$P)Au$^+$](PF$_6^-$), respectively, in dichloromethane solution. Deprotonation of (**4**$^+$)(PF$_6^-$) with KOH in methyl alcohol solution afforded **5**, while complex **6** was prepared by the one-pot reaction of [(TPA)AuCl] with 1 mol of pbiH in the presence of KOH in a MeCN/H$_2$O mixture. The binuclear compound **7** was synthesized by the direct reaction of the mononuclear adduct **1** with [(THT)AuCl], while reaction of **1** and **2** with [(Ph$_3$P)Au$^+$](PF$_6^-$) afforded (**8**$^+$)(PF$_6^-$) and (**9**$^+$)(PF$_6^-$), respectively. Quite unusually,[32] binuclear complexes **7**−**9**$^+$ display pbi$^-$ as a μ_3-bridging ligand between two metal centers in different formal oxidation states, Au^{I} and Au^{III}. Reaction of [(Ph$_3$P)Au$^+$](PF$_6^-$) with an equimolar amount of pbiH in the presence of a stoichiometric amount of KOH afforded the dinuclear Au^{I}−Au^{I} compound (**10**$^+$)(PF$_6^-$).[33] The solubility features of complexes **1**−**10**$^+$ have been reported previously.[27] The spectrophotometric monitoring of dilute aqueous solutions in phosphate buffer at room temperature and physiological pH (7.4) over a period of 24 h showed that they are all stable toward reduction of the metal center, and evidence of formation of negligible amounts of colloidal gold was detected in only a few cases. Similar results were found in a strongly reducing environment (sodium ascorbate 10:1 molar ratio), in which most of the compounds were found to be fairly stable, with complex **6** being the most and compound **1** the least stable.[27] Since the aim of this work is the investigation of the electronic structure of complexes **1**−**3**, **4**$^+$, **5**−**7**, and **8**$^+$−**10**$^+$, all measurements were carried out in CH$_2$Cl$_2$, which provides a sufficient solubility for all compounds, is well suited for CV and UV−vis spectroscopy, and whose solvation properties can be accurately modeled theoretically.

Electrochemistry. The pbiH ligand did not show electroactivity in DMF solution,[27] while in CH_2Cl_2 solution two reduction processes at $E_{1/2}$ = −1.04 and −0.03 V vs SCE, attributed to the pyridine and imidazoline fragments, respectively, were reported.[34] The electrochemical properties of compounds **1**−**3**, ($\mathbf{4}^+$)(PF_6^-), **5**−**7**, and ($\mathbf{8}^+$)(PF_6^-)−($\mathbf{10}^+$)(PF_6^-), carried out in DMF, were reported previously.[27] Cyclic voltammetry (CV) measurements were repeated in CH_2Cl_2 solution, with tetrabutylammonium tetrafluoroborate as a supporting electrolyte (Table 1), and overall confirm the electrochemical properties determined in DMF.

Table 1. Cyclic Voltammetry[a] Data *E* (vs Fc^+/Fc) Recorded at a Platinum Electrode, Excitation and Emission Wavelengths λ_{exc} and λ_{em}, and Quantum Yields Φ Determined for 1−3, 4^+, 5−7, and 8^+−10^+ in CH_2Cl_2 Solution

	E_{pc}/V	E_{pa}/V	λ_{exc}/nm	λ_{em}/nm	$10^{-2}\Phi$
1	−0.451, −0.894		310	370, 410	0.8[d]
2	−0.649, −0.922		310	360	3.4[d]
3	−1.144[b]	+0.135	320, 370	360, 450	14.5,[d] 5.6[e]
$\mathbf{4}^+$ [c]	−1.410[b]		310	360	2.5[d]
5			310	360	2.2[d]
6			300	370	4.6[d]
7	−0.642, −0.874	+0.224	310, 370	360, 460	6.4,[d] 9.0[f]
$\mathbf{8}^+$ [c]	−0.624, −0.845		320	380[g]	0.7[d]
$\mathbf{9}^+$ [c]	−0.708, −0.895		200	280	n.d.[h]
$\mathbf{10}^+$ [c]			310	360	7.9[d]

[a] Conditions: *T* = 298 K, supporting electrolyte tetrabutylammonium tetrafluoroborate 0.1 M, scan rate 25 mV s^{-1}, reference electrode Ag/AgCl. [b] Recorded at 100 mV s^{-1}. [c] Isolated as the PF_6^- salt. [d] 2-Aminopyridine standard (in aqueous H_2SO_4 0.1 N). [e] Anthracene standard in ethyl alcohol solution. [f] Quinine sulfate monohydrate standard (in aqueous H_2SO_4 1 N). [g] Resulting from two independent components; see main text. [h] Not determined.

Gold(III) mononuclear complexes show two irreversible reduction steps, occurring at −0.45 and −0.65 V vs Fc^+/Fc and at −0.89 and −0.92 V vs Fc^+/Fc for **1** and **2**, respectively. The former step is ascribable to a Au^{III}−Au^{I} two-electron reduction, while the latter, accompanied by the formation of a thin gold film on the working electrode, is ascribable to a Au^{I}−Au^{0} process. A two-step process for the reduction of Au^{III} to Au^0, especially in the case of π-acceptor ligands capable of stabilizing gold(I) species,[35] was displayed by analogous gold(III) bipyridine adducts in nonaqueous media, the more negative values of reduction potential for compound **2** as those for to **1** being due to the effect of the acetato ligand on the gold(III) center.[36] Gold(I) mononuclear compounds **3** and ($\mathbf{4}^+$)(PF_6^-) show a single cathodic process at −1.14 and −1.41 V vs Fc^+/Fc, respectively, associated, in the case of **3**, with the deposition of a gold film on the electrode surface. The negative value of the reduction process of ($\mathbf{4}^+$)(PF_6^-) in comparison with that observed for **3** could be attributed to the stabilizing effect of PPh_3 with respect to the chloride anion.[27,36] An anodic process was detected only for compound **3** at +0.13 V vs Fc^+/Fc, which could be tentatively attributed to an irreversible Au^{I}−Au^{III} oxidation. Conversely, neutral complexes **5** and **6**, featuring the ligand in the anionic pbi^- form, are not redox-active under the experimental conditions. This suggests a stabilization effect exerted both (i) by the phosphines PPh_3 and TPA, as observed by the comparison of the potentials of the cathodic processes recorded for **3** and ($\mathbf{4}^+$)(PF_6^-) discussed above, and (ii) by the anionic charge on the pbi^- ligand, as suggested by the comparison of the electrochemical properties of ($\mathbf{4}^+$)(PF_6^-) and **5**. The electrochemical behavior of the neutral binuclear mixed-valence compound **7** can be related to that of the mononuclear complexes **1** and **3**. CV measurements carried out on **7** show two cathodic processes with E_{pc} = −0.64 and −0.87 V vs Fc^+/Fc (Au^{III}−Au^{I} and Au^{I}−Au^{0} reductions, respectively). An anodic peak was observed at +0.22 V vs Fc^+/Fc, similar to that discussed in the case of **3**. In the case of the PF_6^- salts of the cationic complexes $\mathbf{8}^+$ and $\mathbf{9}^+$, bearing PPh_3 as an ancillary ligand on Au^{I}, two cathodic peaks were observed at −0.62 and −0.85 V vs Fc^+/Fc for ($\mathbf{8}^+$)(PF_6^-) and −0.71 and −0.90 V vs Fc^+/Fc for ($\mathbf{9}^+$)(PF_6^-). The less negative processes could be ascribed to Au^{III}−Au^{I} reductions and show E_{pc} values comparable to those found for the precursor **1** and **2**, while the processes at −0.85 and −0.90 V vs Fc^+/Fc can be attributed to the reduction of Au^{I} to Au^{0} and confirm the effect of the substitution of chloride with acetate discussed above. Finally, the gold(I) binuclear compound ($\mathbf{10}^+$)(PF_6^-) is not redox-active in the explored potential range, analogous to what was reported above for **5**.

Absorption/Emission UV−Vis Spectroscopy. The absorption spectrum of pbiH in CH_2Cl_2 solution shows two maxima falling at 230 and 312 nm (ε = 12000 and 22500 M^{-1} cm^{-1}, respectively; Figure S1 in the Supporting Information), each featuring a shoulder at about 240 and 325 nm (ε = 9800 and 17800 M^{-1} cm^{-1}, respectively).[37,38] As previously reported,[39] although pbiH is not emissive in the solid state, it features remarkable fluorescence in solution, its intensity being forcefully quenched in strongly polar solvents[38] and depending on the pH in aqueous solution.[40,41] Excitation spectra collected in CH_2Cl_2 solution show a single intense fluorescent emission (λ_{em} 360 nm), whose spectral shape is independent of the concentration (range 8 × 10^{-5}−1.0 × 10^{-3} M) and the excitation wavelength (range 230−340 nm). The highest emission (quantum yield Φ = 0.31) is achieved by exciting the solution of the ligand in correspondence of the shoulder of the most intense peak (λ_{exc} 330 nm, inset in Figure S1).

Mononuclear Au^{III} complexes **1** and **2** show similar absorption spectra (Figure 1 and Figure S2 (Supporting Information), respectively), featuring three main maxima falling at about 230, 310, 370 nm (ε = 21500, 7700, 13100 M^{-1} cm^{-1}

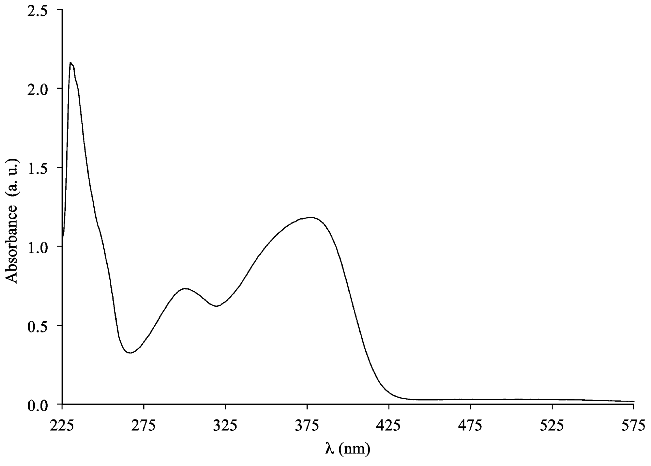

Figure 1. UV−vis absorption spectrum recorded for a CH_2Cl_2 solution of complex **1**. *C* = 1.34 × 10^{-4} M.

for **1**; 12300, 9700, and 5500 M^{-1} cm^{-1} for **2**). The position of the second band corresponds to the excitation wavelength providing the highest emission for both compounds (Table 1). In dilute solution (C up to about 5×10^{-5} M), both **1** and **2** show an emission band centered at 360 nm, remarkably less intense as compared to that of pbiH ($\Phi = 7.9 \times 10^{-3}$ and 3.4×10^{-3} for **1** and **2**, respectively). At higher concentrations, compound **1** exhibits an additional emission band at 410 nm (Figure 2), which could therefore be tentatively attributed to species formed through intermolecular interactions, possibly prevented in the case of **2** by the hindrance of the acetate ligands.

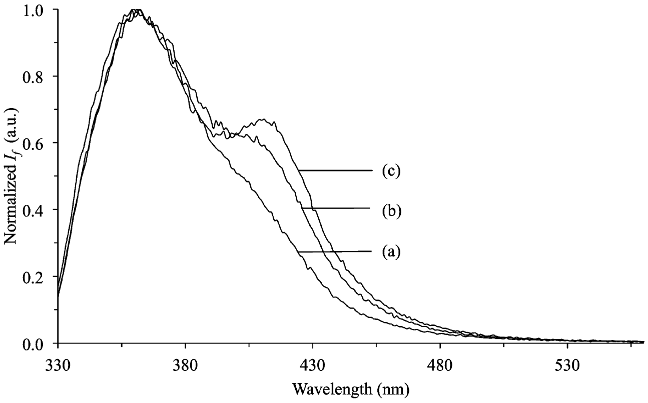

Figure 2. Superimposed normalized emission spectra recorded on CH_2Cl_2 solutions of **1** (λ_{exc} 310 nm): (a) $C = 5.36 \times 10^{-5}$; (b) $C = 1.07 \times 10^{-4}$; (c) $C = 1.34 \times 10^{-4}$ M.

The UV–vis absorption spectra of mononuclear Au^I complexes **3**, (4^+)(PF_6^-), **5**, and **6** (Figures S3–S6, Supporting Information) show two intense groups of bands centered at about 230 and 320 nm for all compounds with molar extinction coefficients in the ranges 13000–28600 and 17500–25000 M^{-1} cm^{-1}, respectively. In the case of **3** a further very weak absorption (ε = 500 M^{-1} cm^{-1}) can be observed at 370 nm. Excitation spectra recorded for **3** are dependent on the concentration of the CH_2Cl_2 solutions. Dilute solutions ($C = 1.0 \times 10^{-4}$ M) show an emission band at 360 nm ($\Phi = 0.145$) achieved with λ_{exc} in the range 220–320 nm. For $C = 10^{-2}$ M, the highest emission is recorded at 450 nm for λ_{exc} 370 nm ($\Phi = 0.056$): i.e., in correspondence of the weakest peculiar absorption band. Notably, aurophilic interactions could be responsible for the emission band at the lowest energy, whose intensity increases in concentrated solutions.

In the case of (4^+)(PF_6^-) and **5** two emission processes were observed, one with emission maxima at 360 nm (Φ = 0.025 and 0.022, respectively) and a very weak one at 460 nm, whose intensity increases with the concentration. This notwithstanding, the intensity of the visible emission is so weak that the corresponding quantum yield could not be determined. Under the hypothesis that aurophilic $Au^I\cdots Au^I$ interactions could be responsible for such low-energy emission, the steric hindrance of the ancillary Ph_3P ligands could justify the very low intensity in comparison to **3**. It is worth noting that the deprotonation of 4^+ to give **5** does not affect significantly either the energy or the intensity of the emission.

The neutral compound **6**, bearing TPA instead of PPh_3, displays a single emission band at 370 nm (λ_{exc} 300 nm), with a quantum yield value ($\Phi = 0.046$) almost double those determined for (4^+)(PF_6^-) and **5** (Figure S6, Supporting Information). When the concentration of the solution is increased (in the range 7.0×10^{-6}–1.7×10^{-4} M), the fluorescence intensity is systematically quenched, but no further emission at lower energy was observed.

Compound **7**, bearing both the $Au^{III}Cl_2$ and Au^ICl moieties joined by a pbi^- unit, shows an UV–vis spectrum in CH_2Cl_2 solution recalling the spectral features of both **1** and **3**, with three main absorption bands centered at 230, 310, and 370 nm (ε = 23000, 21500, 6200 M^{-1} cm^{-1}, respectively; Figure S7, Supporting Information). In analogy with **3**, solutions of **7** are also fluorescent by the naked eye under a UV lamp. Two emission bands were observed at 360 and 460 nm (λ_{exc} 310 and 370 nm, respectively). The quantum yield measurements, carried out independently on the two emission bands, show values of the same order of magnitude ($\Phi = 6.4 \times 10^{-2}$ and 9.0×10^{-2}, respectively). The intensity of the two emission bands shows a peculiar dependence on the concentration, partially analogous to that discussed above for **3**. When the concentration is increased, the emission at 360 nm is quenched, while that at 460 nm undergoes an increase up to about C = 1 mM and then a decrease. This might support the initial formation of a dimer, emitting at 460 nm, held by aurophilic interactions, followed by higher nonemitting aggregates at higher concentrations.

The hexafluorophosphate salts of the complexes 8^+, 9^+, and 10^+ show very similar UV–vis absorption spectra (Figures S8–S10, Supporting Information), with two structured bands falling at about 230 nm (ε = 37980, 37000, and 51100 M^{-1} cm^{-1} for (8^+)(PF_6^-), (9^+)(PF_6^-), and (10^+)(PF_6^-), respectively) and in the range 310–360 nm (ε = 11940, 11700, and 19900 M^{-1} cm^{-1} for (8^+)(PF_6^-), (9^+)(PF_6^-), and (10^+)(PF_6^-), respectively). Dilute solutions ($C = 1.7 \times 10^{-6}$ M) of (8^+)(PF_6^-) show an emission band at 380 nm (λ_{exc} 320 nm). When the concentration is increased, the maximum of the band is shifted toward lower energies (λ_{em} 400 nm for $C = 8.3 \times 10^{-5}$ M, corresponding to the solubility limit in CH_2Cl_2; Figure 3).

Such a shift is in agreement with the presence of two emission bands, one centered at about 360 nm, similarly to what was found for most complexes discussed above, and one at lower energy, possibly due to intermolecular interactions involving the Au^{III} center. Accordingly, a spectral decom-

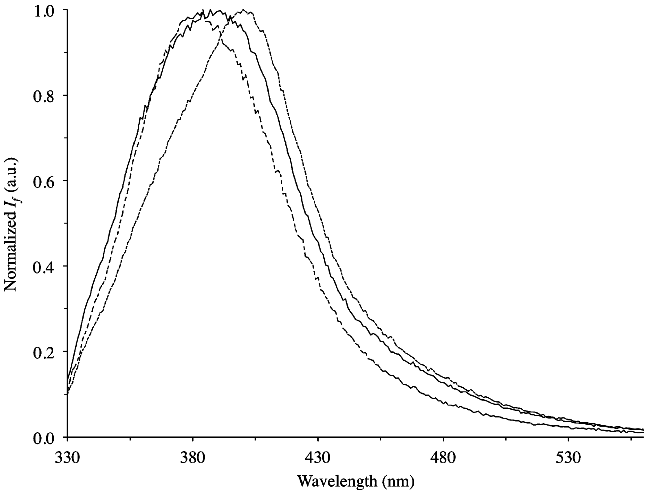

Figure 3. Normalized emission spectra recorded on CH_2Cl_2 solutions of (8^+)(PF_6^-) (λ_{exc} 320 nm): (dotted line) $C = 1.7 \times 10^{-5}$; (continuous line) $C = 5.0 \times 10^{-5}$; (fine-dotted line) $C = 8.3 \times 10^{-5}$ M.

position carried out with Specpeak 2.0[42] on three emission spectra recorded on solutions featuring different solute concentrations shows that all peaks can be decomposed into four Gaussian component curves, centered at λ 373, 422, 484, and 545 nm (full width at half-maximum (fwhm) w = 79.3, 86.6, 94.6, and 30.4 nm, respectively). When the concentration is increased, the first two peaks, corresponding to the emission at higher energy, undergo a decrease in their heights, while the last two, corresponding to the emission at lower energy, endure a continuous increase, thus accounting for the progressive shift of the resulting emission band toward lower energies.

While (9^+)(PF_6^-) does not exhibit a well-defined emission but only a very weak band at about 280 nm (λ_{exc} 200 nm), the binuclear Au^I–Au^I derivative ($\mathbf{10}^+$)(PF_6^-) shows a single emission band at 360 nm (λ_{exc} 310 nm; $\Phi = 7.90 \cdot 10^{-2}$).

These results reveal the following.

(1) Almost all compounds in dilute CH_2Cl_2 solution (5.0×10^{-5} M < C < 1.0×10^{-4} M) show an emission band at about 360 nm: i.e., at the same emission wavelength featured by the uncoordinated pbiH ligand. This suggests that relaxation occurs from excited states laying at similar energies for pbiH, **1**–**3**, $\mathbf{4}^+$, **5**–**7**, and $\mathbf{10}^+$.

(2) The quantum yield values of the emission at 360 nm indicate that coordination to the metal center results in a quenching of the emission, whatever the oxidation state of the gold center.

(3) An emission at lower energy (410–460 nm) appears in less dilute solutions ($C \geq 1.0 \times 10^{-4}$ M) for complexes **1**, **3**, **7**, and $\mathbf{8}^+$: i.e., those complexes featuring chloride ligands. This effect might be tentatively related to the capability of these complexes to establish intermolecular interactions, which would be prevented by the more bulky acetato or phosphino ligands. It is worth underlining that this low-energy emission is independent of the oxidation state of the metal and hence of the planarity of the ligand, which is forced only in Au^{III} complexes. Hence, it is unlikely that conformational relaxation, involved in the emission processes of the dication $(pbiH_3)^{2+}$ in acidic media,[41] plays a part in the emission process.

Theoretical Calculations. The availability of a complete set of structural, spectroscopic, and electrochemical data for the gold complexes discussed in this work provides a challenging opportunity for an in-depth investigation on the electronic features of this class of compounds by quantum-mechanics calculations carried out in the framework of density functional theory (DFT). In order to individuate a computational setup suitable for the investigated complexes, three different functionals have been tested: namely, the well-known hybrid three-parameter B3LYP,[43] mPW1PW,[44] and PBE0[45] (PBE1PBE) functionals. It is largely acknowledged that relativistic effects rule the behavior and reactivity of gold complexes.[46] Hence, four basis sets featuring relativistic effective core potentials (RECPs) have been tested for the heaviest gold center: i.e., CRENBL,[47] LANL08(f),[48] SBKJC,[49] and Stuttgart RLC.[50] All 12 combinations of functionals and basis sets (BSs) with RECPs were tested on complex **7**, which incorporates both a Au^I and Au^{III} center and whose crystal structure was resolved recently.[27] In agreement with recent results on different compounds featuring emitting properties,[51] a comparison between the structural data and the corresponding bond lengths and angles calculated with each computational setup allowed us to conclude that the use of the PBE0 hybrid functional coupled to the LANL08 triple-ζ basis sets, augmented with an f-type polarization function for valence electrons for the heavy Au atomic species, provides the more convenient setup for modeling the gold environment and was consequently extended to all of the investigated compounds (Table S1, Supporting Information).

The geometries of all compounds were optimized both in the gas phase and in the presence of CH_2Cl_2, accounted for implicitly by using the polarizable continuum model (PCM) in its integral equation formalism variant (IEF-PCM).[52]

Complexes **2** and $\mathbf{9}^+$ were optimized with two different orientations of the acetate ligands, one featuring the two groups disposed on the same side and the other on opposite sides with respect to the plane of the pbi$^-$ ligand. Both orientations were indeed shown to be isoenergetic (the energy difference being less than 0.1 mkcal mol^{-1}), did not show negative vibrational frequencies, and did not differ in their ground state (GS) description. In the case of **3**, the effect of the rotation of the noncoordinating pyridine ligand has been investigated.

A scan of the potential energy surface described by the rotation of the pyridine around the C7–C8 bond (Figure 4) shows a modest rotational barrier. The most stable geometry (adopted in the subsequent calculations) is that featuring the pyridine laying on the plane of the benzimidazole moiety with the N3 atom laying on the same side as the N1 atom (C_s point group; dihedral N1–C7–C8–N3 τ = 0°; Chart 1). The opposite disposition (τ = 180°) is higher in the total electronic energy by about 9 kcal mol^{-1}, while the least stable conformation is that displaying the pyridine ring perpendicular to the benzimidazole moiety (ΔE = 11.0 kcal mol^{-1}).

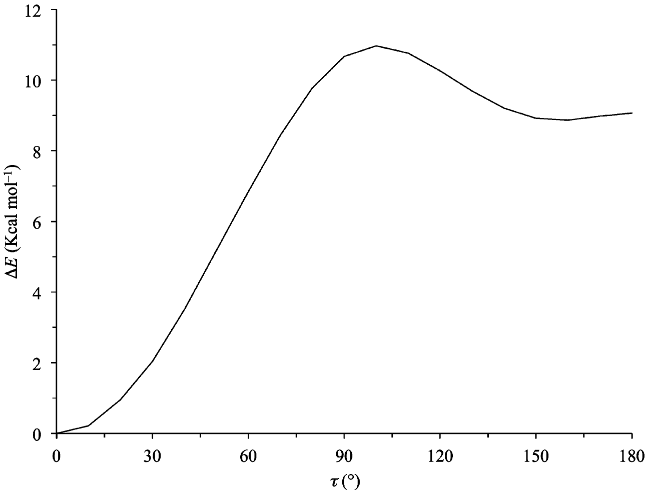

Figure 4. Relative variation of the total electronic energy ΔE as a function of the rotation of the pyridine ring in compound **3** (τ = dihedral N1–C7–C8–N3, Chart 1).

Since emission spectroscopy suggested the presence of dimers in solutions for **3**, the geometry of the dimeric compound $(\mathbf{3})_2$ was also optimized. The dimer shows a head-to-tail geometry with a calculated Au···Au distance of 3.630 Å in CH_2Cl_2 solution. The long interatomic Au···Au distance, the Wiberg bond index[53] (WBI) of 0.083 for the same interaction, and the stabilization in the total electronic energy of $(\mathbf{3})_2$ by 5.83 kcal mol^{-1} with respect to two independent units of **3** clearly indicate that the dimer formation is only moderately favored in CH_2Cl_2 solution.

On the basis of the results obtained for complex **3**, the geometry optimizations of complexes $\mathbf{4}^+$ and **5** were carried out starting from the conformation showing the pyridine ring disposed as in the case of **3**, which led to a roughly planar geometry for the pbiH ligand in the case of **4**$^+$ (τ = 4.62°), while in the case of **5** the rotational barrier is lowered further and the pyridine ligand is rotated by 42.44° at the optimized geometry.[54] The geometry of complex **6** was instead calculated to be planar, in agreement with the crystal structure determination (optimized τ = 179.80°).[27] This geometry results in a short Au1−N3 distance (optimized value 2.702; structural 2.70(1) Å), largely below the sum of the relevant van der Waals radii, indicating an interaction between the pyridine lone pair and the gold(I) ion, as testified by the Wiberg bond index[53] ($\mathrm{WBI}_{\mathrm{Au-N}}$ = 0.102). Accordingly, a second-order perturbation theory analysis of the Fock matrix in the NBO[55] basis shows that such an interaction involves 10.62 kcal mol^{-1} in the gas phase: i.e., an amount large enough to overcome the rotational barrier of the pyridine.

The geometries of the dinuclear complexes **7** and **8**$^+$ are forcedly defined by the coordination to the gold centers, while in the case of the dinuclear Au$^{\mathrm{I}}$ complex **10**$^+$ the pyridine unit is rotated by 22.10°, again in good agreement with the structural values (18.2(4)°). As described above for complex **6**, the geometry of the complex **10**$^+$ results in a short Au1−N3 contact (structural 2.691 Å; optimized 2.798 Å; $\mathrm{WBI}_{\mathrm{Au-N}}$ = 0.079; 8.67 kcal mol^{-1}).

Notably, in the case of **6**, **7**, and **10**$^+$ optimized metric parameters are in very good agreement with the structural data reported previously.[27] In Figure 5 structural bond distances involving the gold ions in compounds **6**, **7**, and **10**$^+$ are compared with the corresponding optimized values. The couples of data are finely correlated (R^2 = 0.98). A comparison of the optimized bond distances and angles calculated in the gas phase and those calculated in CH_2Cl_2 solution (Table S2, Supporting Information) shows that solvation only marginally affects the geometries of the investigated compounds.

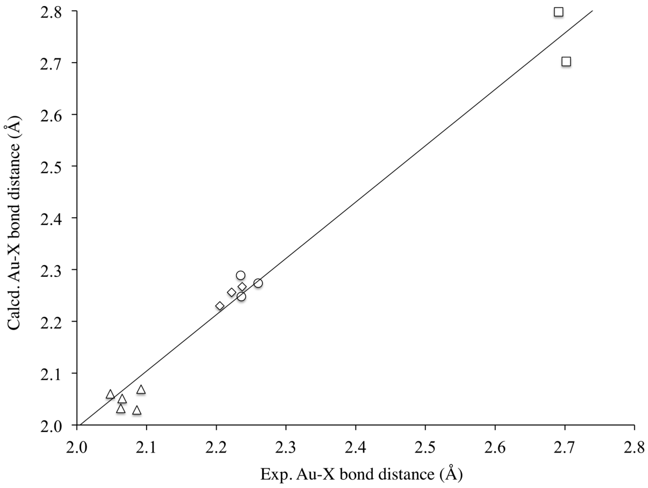

Figure 5. Correlation between structural and optimized Au−X bond distances in complexes **6**, **7**, and **10**$^+$ (X = donor atom): (△) N bonds; (□) N contacts; (○) Cl; (◇) P. Structural values are taken from ref 27. Linear regression parameters: slope 1.09, intercept −0.182 Å, R^2 = 0.98.

An insight into the electrochemical and spectroscopic properties of the gold complexes **1**−**3**, **4**$^+$, **5**−**7**, and **8**$^+$−**10**$^+$ can be achieved from the examination of the composition of the Kohn−Sham molecular orbitals (KS−MOs).

In Table 2 the eigenvalues ε calculated for KS-HOMO and KS-LUMO both in the gas phase and in CH_2Cl_2 solution are given. As expected, cationic complexes feature a systematic stabilization of both MOs with respect to neutral complexes, independent of the oxidation state of gold or the nature of the ancillary ligands, partially moderated by solvation.[56] KS-LUMO eigenvalues calculated for **1**−**3**, **4**$^+$, **5**−**7**, and **8**$^+$−**10**$^+$ at the IEF-SCRF level can be compared with the reduction cathodic potentials measured by CV (Table 1), although the changes in the thermodynamic parameters involved in the redox process leading to differently charged species are neglected.[57] Qualitatively, more negative $\varepsilon_{\mathrm{LUMO}}$ values indicate a higher stabilization of the reduced species and hence an easier reduction reflected in less negative E_{pc} values.

Table 2. KS-HOMO and LUMO Eigenvalues ε Calculated for pbiH and 1−3, 4$^+$, 5−7, and 8$^+$−10$^+$ in the Gas Phase and in CH_2Cl_2

	$\varepsilon_{\mathrm{HOMO}}$/eV		$\varepsilon_{\mathrm{LUMO}}$/eV	
	gas	CH_2Cl_2	gas	CH_2Cl_2
pbiH	−6.297	−6.476	−1.561	−1.650
1	−6.611	−6.696	−3.426	−3.471
2	−6.742	−6.744	−2.962	−2.810
3	−6.463	−6.899	−2.410	−2.176
4$^+$	−9.457	−7.315	−4.689	−2.484
5	−5.471	−6.095	−1.531	−1.284
6	−5.541	−6.059	−1.146	−1.421
7	−6.750	−6.961	−4.045	−3.749
8$^+$	−9.571	−7.473	−5.993	−3.984
9$^+$	−9.367	−7.516	−5.537	−3.282
10$^+$	−8.487	−6.899	−3.836	−2.078

An examination of Figure 6 shows that indeed the reduction potentials E_{pc} of neutral and cationic complexes are, with the only exception of **4**$^+$, qualitatively related with the corresponding $\varepsilon_{\mathrm{LUMO}}$ values calculated within the SCRF approach of solvation.

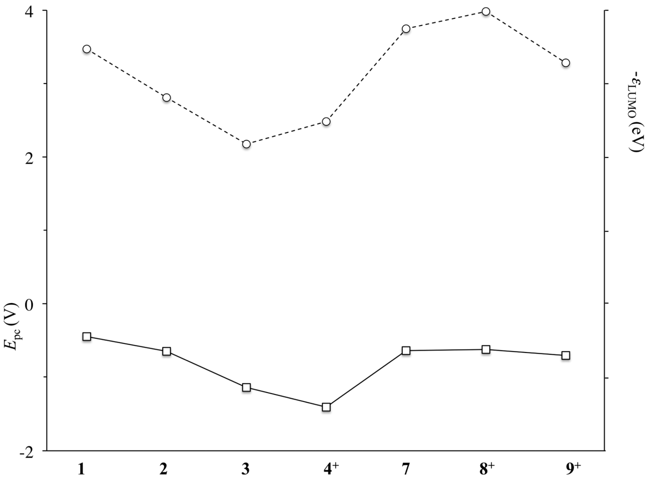

Figure 6. Cathodic potential of the first reduction processes E_{pc} measured by CV in CH_2Cl_2 solution (□; Table 1) compared with the KS-LUMO eigenvalues calculated at the IEF-SCRF DFT level in the same solvent (○; Table 2) for **1**−**3**, **4**$^+$, **7**, **8**$^+$, and **9**$^+$.

For all complexes in CH_2Cl_2 solution, KS-HOMO is an antibonding π in nature MO localized on the benzimidazole moiety of the pbiH/pbi$^-$ ligand, whose composition corresponds in the case of **1**–**3**, **4**$^+$, **5**, **6**, and **10**$^+$ to that of the KS-HOMO of the free pbiH ligand calculated at the same level of theory (Figure 7 for **1**, **3**, and **7**). In the case of 7, **8**$^+$, and **9**$^+$, KS-HOMOs show the ligand contributing with its HOMO-1. Notably, only in the case of the complexes featuring Au^I–Cl moieties (**3** and **7**) does the metal participate in the HOMO with its 5d$_{yz}$ atomic orbitals (AOs).

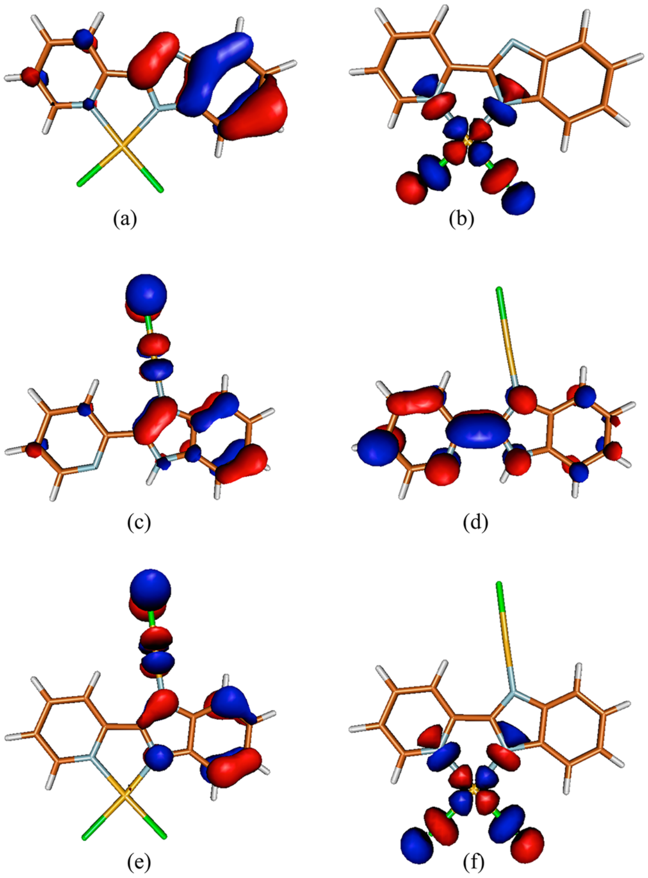

Figure 7. KS-HOMO (left) and LUMO (right) isosurfaces calculated for **1** (a, b), **3** (c, d), and **7** (e, f) in CH$_2$Cl$_2$ solution. Cutoff value 0.05e.

In the case of all Au^{III} complexes (**1**, **2**, **7**, **8**$^+$, and **9**$^+$), KS-LUMOs are built up by the σ-antibonding interaction between the in-plane 5d$_{xy}$ AOs of the metal center interacting with the four donor atoms (Figure 7 for **1**, **3**, and **7**). In contrast, in the case of Au^I complexes, KS-LUMO is localized on the pbi$^-$/pbiH moiety, and its composition coincides with that of the LUMO of pbiH with the only exception of complex **5**, featuring the LUMO localized on the PPh$_3$ ligand.

Interestingly, the composition of the LUMO for Au^{III} complexes **1** and **2** confirms that the first reduction should be considered metal-centered. The antibonding nature of these MOs is in agreement with the irreversibility of the first reduction processes. On passing from X$_1$ = X$_2$ = Cl in **1** to X$_1$ = X$_2$ = AcO in **2**, $\varepsilon_{\text{LUMO}}$ values confirm a destabilization of the MO (by 0.47 and 0.66 eV in the gas phase and in CH$_2$Cl$_2$ solution, respectively), reflected in a shift of E_{pc} toward more negative values. More intricate is the interpretation of the electrochemical data recorded for Au^I complexes. In fact, the composition of LUMOs suggests that the reduction processes of these complexes should be localized on the pbi$^-$/pbiH ligand. This notwithstanding, the energy of the LUMOs of these complexes (Table 2) is dramatically affected not only by the coordination to gold(I) but also by the nature of the ancillary ligand X$_1$ for complexes **3**, **4**$^+$, **5**, and **6** and X$_1$/X$_2$ for complex **10**$^+$ (Chart 1).[58] Possibly, a subsequent CT process is responsible for the reduction of gold, indicated by the formation of a gold film at the cathode.

For mixed-valence Au^I/Au^{III} complexes the first reduction process is centered on the Au^{III} core, as suggested by the E_{pc} values discussed above.

Selected natural charges Q on the Au$^{I/III}$ center and on the donor atoms are summarized in Table 3. Gold(III) complexes **1** and **2** show significantly different charges Q_{Au} on the metal ion, the most negative being achieved in **2**, further confirming the larger donor ability of acetate with respect to chloride. Gold(I) mononuclear complexes **3**–**6** and the binuclear Au^I complex **10**$^+$ feature Q_{Au} values strongly depending on the type of X$_1$ ligand, phosphine donors resulting in more positive Q_{Au} values. In contrast to what was found in the case of the complex [Au(bipy)(η^2-CH$_2$=CH$_2$)]$^+$,[59] featuring the Au^I center in a different coordination geometry, in the case of the gold(I) complexes discussed here the positive natural charge on the metal ion should not involve remarkable back-bonding to the phosphine ligands. In fact, a second-order perturbation theory analysis of the Fock matrix in the NBO basis does not show any significant charge transfer from the metal to the phosphine ligands, which carry a large net positive charge (0.456, 0.341, and 0.322 for **4**$^+$, **5**, and **6**, respectively). Indeed, linearly coordinated Au^I complexes are considered not to be suitable to

Table 3. Selected Natural Charges Q (in e) Calculated on pbiH and Complexes 1–3, 4$^+$, 5–7, and 8$^+$–10$^+$ in the Gas Phase[a]

	Q_{N1}	Q_{N2}	Q_{N3}	Q_{Au1}	Q_{Au2}
pbiH	−0.576 (−0.570)	−0.525 (−0.552)	−0.513 (−0.519)		
1	−0.563 (−0.560)	−0.498 (−0.522)	−0.491 (−0.481)	0.711 (−0.763)	
2	−0.582 (−0.576)	−0.495 (−0.522)	−0.506 (−0.495)	1.107 (−1.152)	
3	−0.555 (−0.544)	−0.581 (−0.594)	−0.516 (−0.516)	0.246 (−0.276)	
4$^+$	−0.542 (−0.538)	−0.635 (−0.632)	−0.507 (−0.512)	0.321 (−0.356)	
5	−0.511 (−0.560)	−0.711 (−0.700)	−0.455 (−0.491)	0.322 (−0.333)	
6	−0.543 (−0.577)	−0.677 (−0.675)	−0.509 (−0.512)	0.302 (−0.300)	
7	−0.546 (−0.539)	−0.567 (−0.579)	−0.488 (−0.477)	0.716 (−0.777)	0.249 (−0.282)
8$^+$	−0.536 (−0.534)	−0.627 (−0.614)	−0.487 (−0.476)	0.713 (−0.779)	0.318 (−0.340)
9$^+$	−0.550 (−0.552)	−0.628 (−0.618)	−0.497 (−0.488)	1.120 (−1.159)	0.319 (−0.357)
10$^+$	−0.633 (−0.640)	−0.659 (−0.656)	−0.495 (−0.500)	0.330 (−0.340)	0.320 (−0.346)

[a] The corresponding values calculated in CH$_2$Cl$_2$ at the IEF-SCRF DFT level are reported in parentheses. Atom labeling is given as in Chart 1.

participate in Chatt–Dewar–Duncanson-type bonding[60] due to the energy mismatch between filled 5d orbitals on the metal and empty antibonding MOs of π-acid ligands.[46]

On passing to binuclear mixed-valence gold compounds **7**, **8**$^+$, and **9**$^+$, Q_{Au} charges are clearly determined by the local coordination of the metal ions. Accordingly, the natural charge on the Au^I center (Q_{Au1}) in **7** is very close to the value calculated for **3**, and analogously the Q_{Au1} values in **8**$^+$ and **9**$^+$ are very close to the corresponding values calculated for **4**$^+$ and **5**.

Time-dependent DFT (TD-DFT) calculations were performed at the same level of theory discussed above on pbiH and complexes **1**–**3**, **4**$^+$, **5**–**7**, and **8**$^+$–**10**$^+$ in their GS optimized geometries both in the gas phase and in CH_2Cl_2. In general, a comparison between experimental UV–vis spectra and those calculated on the basis of vertical singlet excitation energies E_{PBE0} and oscillator strengths f shows a very good agreement, as a further confirmation of the choice of computational setup and solvation model. A detailed analysis of the TD-DFT data for all of the examined compounds is beyond the scope of this work. Hence, only the data related to the free pbiH ligand, the Au^{III} complex **1**, the Au^I complex **3**, and the Au^I/Au^{III} mixed-valence complex **7** will be discussed.

The convolution of the main transitions ($f > 0.015$; Table S3, Supporting Information) calculated for pbiH in CH_2Cl_2 results in a simulated spectrum showing two maxima, whose wavelengths and intensity ratio (λ_{max} 206 and 297 nm; oscillator strength ratio 2.65, respectively) are in good agreement with the experimental spectral data recorded in the same solvent (Figures S1 and S11, Supporting Information). The most intense transition ($f = 0.846$) is calculated to fall at $E_{PBE0} = 4.167$ eV (S0 → S1, Figure 9c). This transition largely involves a HOMO–LUMO monoelectronic excitation and corresponds to a charge transfer from the benzimidazole to the pyridine moiety of the ligand. Hence, the radiative relaxation from S1 should be considered responsible for the intense luminescence of pbiH at 360 nm.

In Tables S4–S6 (Supporting Information) the calculated energies and wavelengths, the oscillator strengths, and the singlet excited states involved in the main vertical transitions calculated for **1**, **3**, and **7** are summarized. The corresponding simulated absorption spectra based on IEF-PCM SCRF TD-DFT calculations are represented in Figure 8.

The absorption spectrum simulated for **1** in CH_2Cl_2 (Figure 8a) shows three groups of bands, whose overlap determines three maxima at 203, 287, and 355 nm, the energies of which are slightly overestimated with respect to the corresponding experimental values (Figure 1). The band at lower energy (E_{PBE0} = 3.493 eV) originates in several singlet transitions (Figure 9a). An examination of the monoelectronic excitations contributing to each electronic transition shows that the most intense transition (S1 → S6; $f = 0.223$; Table S4, Supporting Information) originates in HOMO → LUMO+1 and HOMO-1 → LUMO+1 excitations involving π in nature MOs entirely localized on the pbi$^-$ ligand. This notwithstanding, the S0 → S7 transition, albeit less intense ($f = 0.096$), involves the HOMO-6 and LUMO (Figure 7b), which are σ-MOs partly localized on the Au^{III} center, showing a remarkable contribution from the $5d_{x^2-y^2}$ and $5d_{xy}$ AOs, respectively. The second weak absorption band at about 4.320 eV is mainly determined by the S0 → S10 transition ($f = 0.131$; Figure 9a), in turn due to a large contribution of the HOMO → LUMO+2 excitation only involving MOs localized on the ligand.

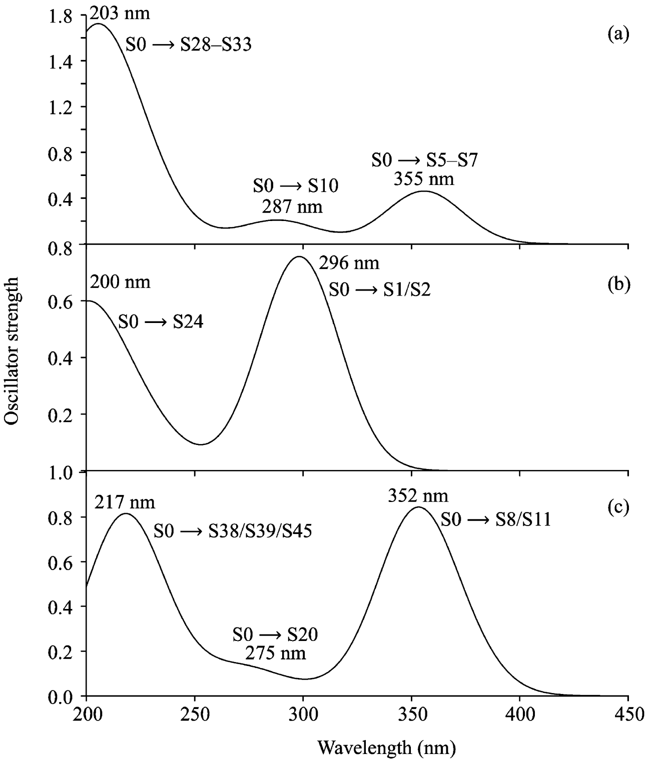

Figure 8. Simulated UV–vis spectra (180–450 nm) for complexes **1** (a), **3** (b), and **7** (c) in CH_2Cl_2 solution based on IEF-PCM SCRF TD-DFT calculations. The main vertical singlet transitions contributing to the absorptions are indicated along with the resulting maxima wavelengths. No further absorption is calculated beyond 450 nm.

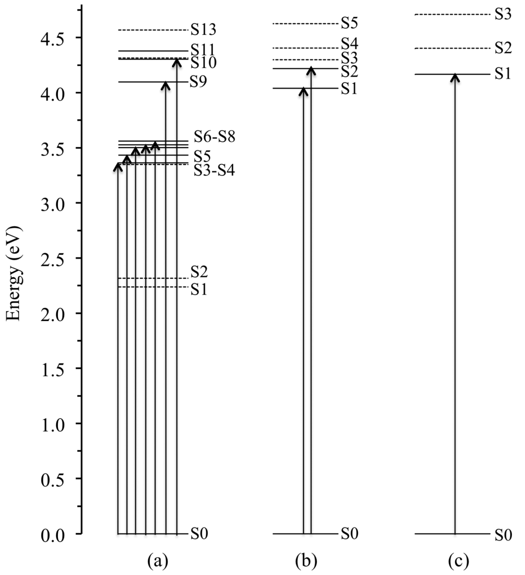

Figure 9. Diagram showing the relative energies of the singlet excited states with respect to the ground states S0 calculated for complexes **1** (a) and **3** (b) and for the free ligand pbiH (c) in CH_2Cl_2 solution on the basis of IEF-PCM SCRF TD-DFT calculations. The singlet excited states with oscillator strength values $f < 0.015$ are represented as dotted lines.

The most intense band of the simulated spectrum falls at 6.108 eV and is due to the overlap of several transitions, the most intense of which implicate the singlet excited states between S28 and S33 (E_{PBE0} = 5.816 and 6.180 eV, respectively). Interestingly, the S0 → S30 and the S0 → S32 transitions are contributed by the HOMO-13 → LUMO and HOMO-5 → LUMO+2 excitations, respectively, which involve MOs largely localized on the gold 5d AOs. In agreement with the UV−vis spectroscopic data, the simulated absorption spectrum of **3** (Figure 8b and Table S5 (Supporting Information)) closely recalls that calculated for pbiH (Figure S11, Supporting Information) and features two groups of bands centered at 4.189 and 6.199 eV, respectively. The band at the lowest energy derives from the S0 → S1 and S0 → S2 transitions (Figure 9b; E_{PBE0} = 4.039 and 4.219 eV; f = 0.296 and 0.509, respectively), which are due to HOMO → LUMO and HOMO-1 → LUMO monoelectronic excitations, showing a MLCT nature. This notwithstanding, since KS-HOMO and LUMO calculated for **3** show large contributions from the HOMO and LUMO of the pbiH ligand, the energies of the transitions in pbiH and **3** are very similar. The absorption at about 200 nm mainly originates in the S0 → S24 transition (E_{PBE0} = 6.250 eV, f = 0.182), in turn consisting of HOMO → LUMO+3, HOMO-1 → LUMO+2, and HOMO-4 → LUMO+2 excitations. LUMO+2 and LUMO+3 are π-MOs localized on the benzimidazole moiety of the pbiH ligand; therefore, this transition should be considered partially MLCT in nature as well.[61]

In the simulated spectrum calculated for **7** (Figure 8c and Table S6 (Supporting Information)) in CH_2Cl_2 the absorption at about 350 nm derives from the S0 → S8 (E_{PBE0} = 3.340 eV; f = 0.104) and S0 → S11 (E_{PBE0} = 3.553 eV; f = 0.366) transitions, corresponding to HOMO → LUMO+1 and HOMO-1 → LUMO+1 monoelectronic excitations. The electronic transition S0 → S19 (E_{PBE0} = 4.526 eV; f = 0.091) is the main component to the weak shoulder at about 275 nm and has the same nature as the similar weak band calculated at the very same energy for **1** (HOMO-1 → LUMO+2 excitation, centered on the pbi$^-$ ligand). The intense absorption calculated at about 220 nm (5.714 eV) arises from three main transitions, namely S0 → S38 (E_{PBE0} = 5.626 eV, f = 0.144), S0 → S39 (E_{PBE0} = 5.684 eV, f = 0.226), and S0 → S45 (E_{PBE0} = 5.842 eV, f = 0.225), each of which is contributed by several monoelectronic MLCT excitations and involves both the Au$^{\mathrm{I}}$ (for example HOMO-12 → LUMO+1 contributes to the S0 → S38 transition with an excitation from the Au$^{\mathrm{I}}$ 5d$_{xz}$ to the benzene ring of the pbi$^-$ ligand) and Au$^{\mathrm{III}}$ centers.

A comparison between the calculated transition energies E_{PBE0} and the experimental absorption energies E_{exp} calculated from absorption spectra recorded for **1**, **3**, and **7** (Table S7, Supporting Information) shows that the sets of data can be exploited for developing a simple linear correction scheme (Figure S12 (Supporting Information), R^2 = 0.98) for IEF-PCM SCRF TD-DFT transition energies calculated with the PBE0 functional (eq 1).

$$E_{\mathrm{best}} = 0.485 + 0.811E_{\mathrm{PBE0}} \tag{1}$$

By adoption of the corrected transition energies E_{best}, the corresponding λ_{best} wavelengths calculated for **1**, **3**, and **7** show a difference $\Delta\lambda$ with respect to the experimental values falling in the range 1−12 nm (Table S7, Supporting Information).

The emission properties of complexes **1**−**3**, **4**$^+$, **5**−**7**, and **8**$^+$−**10**$^+$, at least in dilute solutions, can be investigated on the basis of TD-DFT calculations. In this context, complexes **1** and **3** can be considered as models of all Au$^{\mathrm{III}}$ and Au$^{\mathrm{I}}$ complexes, respectively.

It has been reported above that the maximum emission of complex **1** is achieved when the complex undergoes excitation at 310 nm (Table 1), i.e. corresponding to the S0 → S10 band (Figures 8 and 9) that is calculated at 4.320 eV (corrected value 311 nm; Table S7, Supporting Information) and corresponds to the excitation of ligand-centered MOs. Since ESs with energies higher than S9 are all very close in energy (Figure 9a), it is likely that relaxation from these states leads to the S9 state through an internal conversion (IC) process. In contrast, the energy difference between the S9 and S8 states (0.206 eV) would prevent a fast IC, resulting in the fluorescent emission S9 → S0, whose energy would be similar to that featured by pbiH, in apparent violation of Kasha's rule.[62]

The gold(I) complex **3** features an emission at the same energy (Table 1). The emission can be tentatively attributed to the S1 → S0 process (Figure 9b). Excitation to higher excited states would result in an IC process to S1, followed by fluorescent relaxation to S0.

TD-DFT calculations were extended to the pattern of triplet excited states. As expected, all complexes feature a complex pattern of triplet states featuring energies matching those of the singlet excited states. In Figure 10 a Jablonski diagram representing singlet (S) and triplet (T) ESs calculated for **1** is depicted. The singlet ESs accessible from the GS with the largest values of oscillator strengths f, and in particular S6, S9, and S10, feature triplet ESs (T9 and T15−T17, respectively) very close to each other in energy. The spin-forbidden ISC process occurs through the interaction between the electronic spin and orbital moments. Since the spin−orbit coupling constant depends on the fourth power of the effective nuclear charge,[63] ISC is enhanced in systems containing heavy atoms.[64] The rate of ISC strongly depends on the overlap between the vibrational wave functions of the involved singlet and the triplet

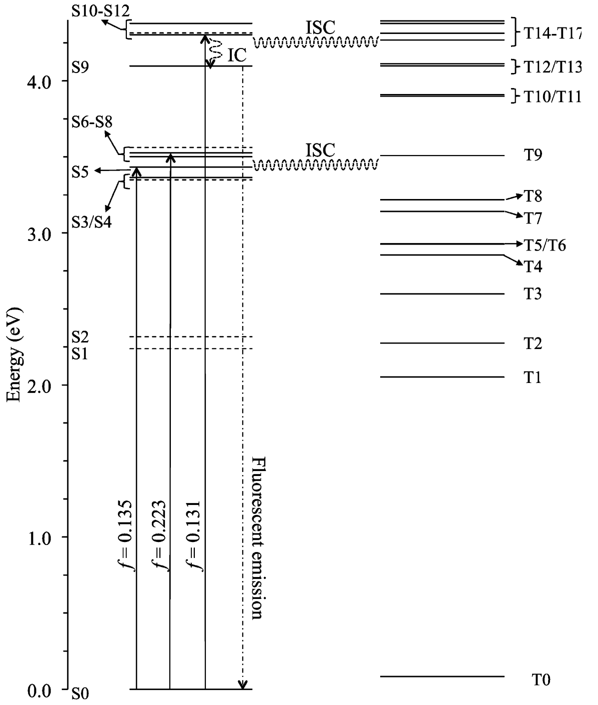

Figure 10. Jablonski diagram (0.0−4.4 eV; uncorrected transition energies) calculated for **1** in CH_2Cl_2 by IEF-PCM SCRF TD-DFT calculations. The singlet excited state transitions with oscillator strength values f < 0.015 are represented as dotted lines.

states; thus, pairs of singlet and triplet quasi-degenerate states are good candidates to participate in ISC processes. Selection rules for SO coupling operator require that the direct product of the irreducible representation of $^1\psi$ and $^3\psi$, the initial and final states involved in the ISC process, respectively, must contain the irreducible representation of at least one of the three components of the orbital moment operator L. Since in the C_s point group all excited states belong to either the A′ or A″ representations, and therefore the direct product of their representations contains necessarily one or two of the components of L, all ISC processes are in all cases allowed by orbital symmetry-based selection rules.[65] Therefore, although the measurement and calculation of ISC rates[66] are outside the goals of this research, in agreement with the fluorescence measurements discussed above (Table 1), ISC may reasonably provide an alternative relaxation path with respect to fluorescence, thus accounting for the lower quantum yields determined for all complexes **1**−**3**, **4**$^+$, **5**−**7**, and **8**$^+$−**10**$^+$ in comparison to that of the pbiH ligand.

CONCLUSIONS

A combined experimental and theoretical approach has been exploited to investigate the electronic structure of the series of 10 gold complexes **1**−**3**, **4**$^+$, **5**−**7**, and **8**$^+$−**10**$^+$ deriving from pbiH and different ancillary ligands and showing remarkable antiproliferative properties toward A2780 human ovarian carcinoma cells. Cyclic voltammetry measurements demonstrate that the title complexes are stable toward reduction to gold(0) over a large range of applied potentials. In dilute solutions, all compounds but **9**$^+$ show a peculiar emission at about 360 nm, typical of the pbiH ligand, quenched with respect to the free ligand. The emission at lower energies (410−450 nm) shown by several complexes suggests that intermolecular interactions possibly occur, although theoretical calculations carried out on the dimer $(\mathbf{3})_2$ indicate a very weak $\mathrm{Au^I\cdots Au^I}$ interaction.

A precise choice of the DFT computational setup, and in particular of the functional and the basis set for the gold atom, accounting for relativistic effects peculiar to this element, is reflected in well-predicted metric parameters, also indicated by the agreement between the potentials of the cathodic peaks and KS-LUMO eigenvalues. TD-DFT calculations allow for an in-depth understanding of the excitation processes determining the UV−vis spectra. In particular, the pattern of singlet and triplet excited states clarifies the nature of emission processes and relaxation paths.

The accurate modeling of the electronic structure of the gold complexes **1**−**3**, **4**$^+$, **5**−**7**, and **8**$^+$−**10**$^+$ supports an attempt to explain the antiproliferative effects shown against cisplatin-sensitive (S) and -resistant (R) A2780 ovarian cancer cell lines in light of DFT calculations. In Figure S13 (Supporting Information) and Figure 11 (top), $\varepsilon_{\mathrm{LUMO}}$ eigenvalues, calculated in the gas phase (Table 2), are compared with $\mathrm{IC_{50}}$ values determined for the A2780/S and A2780/R cell lines, respectively, after 72 h of exposure to the title gold complexes.[27] With the only exception of **5**, a tentative logarithmic correlation holds (Figure 11 bottom),[67,68] the largest antiproliferative effect (and hence the lowest $\mathrm{IC_{50}}$ value) being shown by the compounds showing the lowest eigenvalues calculated for KS-LUMO. In particular, the following can be concluded.

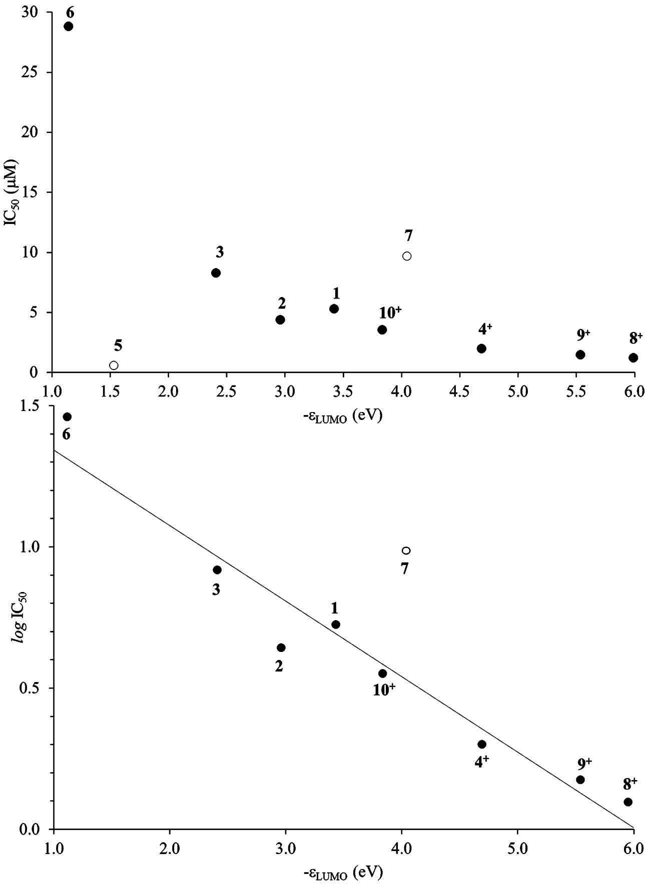

Figure 11. (top) Comparison between $\mathrm{IC_{50}}$ values measured for the A2780/R cell line and the KS-LUMO eigenvalues $\varepsilon_{\mathrm{LUMO}}$ calculated for **1**−**3**, **4**$^+$, **6**, **7**, and **8**$^+$−**10**$^+$ in the gas phase (Table 2). (bottom) Least-squares fit (slope $-0.267\ \mathrm{eV^{-1}}$, intercept 1.610; $R^2 = 0.95$). Data for **5** and **7** (unfilled circles) have been considered anomalies and are not included in the fit. $\mathrm{IC_{50}}$ values are taken from ref 27.

(1) Cationic complexes show systematically lower $\varepsilon_{\mathrm{LUMO}}$ eigenvalues and lower $\mathrm{IC_{50}}$ values in comparison to those of neutral complexes.

(2) Dinuclear mixed-valence $\mathrm{Au^I/Au^{III}}$ complexes show lower $\varepsilon_{\mathrm{LUMO}}$ and $\mathrm{IC_{50}}$ values in comparison to those of the corresponding mononuclear complexes. For example, complex **7** shows a stabilization of the LUMO as compared to $\mathrm{Au^I}$ complex **3** and $\mathrm{Au^{III}}$ complex **1**, accompanied by a remarkable decrease in the $\mathrm{IC_{50}}$ value. The LUMO stabilization does not imply a communication between the two metal centers, as proved by electrochemical measurements and DFT calculations.

(3) As previously observed, the presence of $\mathrm{PPh_3}$ ancillary ligands, and therefore the N−Au−$\mathrm{PPh_3}$ moiety, results for all compounds but **5** (the only complex in the series featuring the LUMO not localized on $\mathrm{pbi^-}$) in a stabilization of the LUMO energy and an increase in the cytotoxic properties.

(4) This effect should not be generalized to all phosphines. In fact **6**, featuring the TPA ligand, shows the highest $\mathrm{IC_{50}}$ and $\varepsilon_{\mathrm{LUMO}}$ values. The relative LUMO instability suggests that the high $\mathrm{IC_{50}}$ value should not be attributed to a role played by the hindrance of TPA in the molecular mechanism of antitumor action but rather to the effect of the ligand on the electronic structure of the complex. Furthermore, TPA is known to confer water solubility to metal-based compounds, while $\mathrm{PPh_3}$ confers a lipophilic character. Since the most cytotoxic compounds are

those showing a lipophilic character,[69] this parameter could contribute to the IC$_{50}$ value along with electronic effects.

On the whole, the previous observations support a direct role of the electronic structure of gold complexes derived from the pbiH ligand in their cytotoxicity. Since the title gold complexes proved to be remarkably stable to biologically relevant reducing agents (sodium ascorbate),[27] although no mechanistic conclusion can be drawn at this stage, the relationship between the LUMO stabilization and the cytotoxic activity might support the hypothesis that a charge transfer process, if not a reduction, might be involved in the mechanism of action of **1**−**3**, **4**$^+$, **5**−**7**, and **8**$^+$−**10**$^+$ as antiproliferative agents. This would be in agreement with the relationship between the oxidizing character and the cytotoxic effects reported previously for a series of binuclear μ-oxo Au^{III} complexes.[26]

It is to be remarked that these preliminary findings concern correlations between calculated parameters and the cytotoxicity against only two selected cell lines, and hence caution has to be applied, owing to the extreme complexity of the biological actions of metal-based compounds. In this context, the conclusions drawn here represent only a step which needs further investigation on the cellular effects of these gold compounds and their reactivity toward their expected biomolecular targets (for example, oxidoreductases). This notwithstanding, the quantitative structure−activity relationships outlined here might represent useful guidelines for the design of new potential anticancer drugs based on gold complexes.

■ EXPERIMENTAL SECTION

All reagents were purchased from Sigma-Aldrich and used as received without further purifications. Solvents were dried prior to use according to standard methods. 2-(2′-Pyridyl)benzimidazole (pbiH) and complexes **1**−**3**, (**4**$^+$)(PF$_6^-$), **5**−**7**, and (**8**$^+$)(PF$_6^-$)−(**10**$^+$)(PF$_6^-$) were synthesized as previously reported.[27] Analytical and spectroscopic (FT-IR and ^{1}H, ^{31}P NMR) data obtained for all compounds are in agreement with those reported in the literature. Cyclic voltammetry experiments were recorded using a conventional three-electrode cell, consisting of a combined platinum working and counter electrode and a standard Ag/AgCl (in KCl 3.5 mol L^{-1}; 0.2223 V at 25 °C) reference electrode. The experiments were performed at room temperature under an argon atmosphere in anhydrous CH$_2$Cl$_2$ with Bu$_4$NBF$_4$ (0.1 M) as supporting electrolyte, at a potential scan rate of 0.025 V s^{-1}. Experiments were carried out on a computer-controlled Metrohm Autolab PGSTAT 10 potentiostat−galvanostat using Model GPES electrochemical analysis software. All potential values are referred to the bis(cyclopentadienyl)iron(III)/-iron(II) couple (Fc$^+$/Fc, $E_{1/2}$ = +0.60 V versus Ag/AgCl under experimental conditions). Absorption spectra were recorded on a Thermo Nicolet Evolution 300 spectrophotometer (190−1100 nm) at room temperature using quartz cuvettes with an optical path length of 10.0 mm. Emission and excitation spectra were obtained at room temperature with a Varian Cary Eclipse Fluorescence spectrophotometer (Xe lamp) using quartz cuvettes with an optical path length of 10.0 mm. Spectra were recorded on CH$_2$Cl$_2$ solutions, and luminescence quantum yields were determined for all emitting solutions using an appropriate standard as a quantum yield reference.[70] In particular, anthracene in ethyl alcohol solution (Φ_R = 0.27) was used for the visible emission of complex **3** and quinine sulfate hydrate in aqueous sulfuric acid 1 N (Φ_R = 0.55) was used for **7**, while 2-aminopyridine in sulfuric acid 0.1 N aqueous solution (Φ_R = 0.60) was used in all the remaining cases (see Table 1). The areas of all of the emission spectra were evaluated by using the program Fytik.[71] When the emission spectral shapes undergo significant modification, depending on the concentration of the analyte, a spectral decomposition was carried out by using the Specpeak 2.0 program.[42] Quantum chemical DFT calculations were performed with the commercial suite of software Gaussian09 (rev. A02)[72] on the free ligand pbiH and the complexes **1**−**3**, **4**$^+$, **5**−**7**, and **8**$^+$−**10**$^+$ (Chart 1) at the density functional theory (DFT) level. The computational setup was chosen by testing different functionals (B3LYP,[43] mPW1PW,[44] PBE0[45]) and basis sets with relativistic effective core potentials (RECPs: CRENBL,[47] LANL08(f),[48] SBKJC,[49] and Stuttgart RLC[50]), as discussed above. Eventually all calculations adopted the parameter-free PBE0 functional[45] (implemented as PBE1PBE in Gaussian),[73] combining the so-called PBE generalized gradient functional with a predefinite amount of exact exchange. For all atomic species Schäfer et al. full-electron double-ζ basis sets with polarization functions were used,[74] but for the heavier Au species, for which the triple-ζ LANL08(f) basis set with relativistic effective core potentials (RECPs)[48] was preferred. Basis sets and RECPs were obtained from the EMSL Basis Set Library through the Basis Set Exchange (BSE) software.[75] Geometry optimizations were performed starting from structural data when available. Tight SCF convergence criteria (SCF=tight keyword) and fine numerical integration grids (Integral(FineGrid) keyword) were used, and the nature of the minima of each optimized structure was verified by harmonic frequency calculations (freq=Raman keyword). Natural[55] and Mulliken atomic charge distributions were calculated at the optimized geometries at the same level of theory and electronic transition energies and oscillator strengths were calculated at the TD-DFT level (100 states). The electronic spectra were simulated by a convolution of Gaussian functions centered at the calculated excitation energies (half-bandwidth 20 nm). In order to account for the influence of the solvent on the spectroscopic properties of the model compounds, calculations were also carried out in the presence of CH$_2$Cl$_2$, implicitly taken into account by means of the polarizable continuum model (PCM) approach (linear response; nonequilibrium solvation) in its integral equation formalism variant (IEF-PCM), which describes the cavity of the solute within the reaction field (SCRF) through a set of overlapping spheres.[52] The program Molden 5.0[76] was used to investigate the charge distributions and molecular orbital shapes.

■ ASSOCIATED CONTENT

Ⓢ Supporting Information

Figures and tables giving absorption and emission spectra for pbiH and **1**−**3**, (**4**$^+$)(PF$_6^-$), **5**−**7**, and (**8**$^+$)(PF$_6^-$)−(**10**$^+$)(PF$_6^-$), a simulated absorption spectrum for pbiH, a correlation between experimental and calculated transition energies, a comparison between $\varepsilon_{\text{LUMO}}$ and IC$_{50}$ values, calculated metric parameters at the DFT level, and details of TD-DFT calculations. This material is available free of charge via the Internet at http://pubs.acs.org.

■ AUTHOR INFORMATION

Corresponding Author

*E-mail for M.A.: marca@unica.it.

Notes

The authors declare no competing financial interest.

■ ACKNOWLEDGMENTS

L.M. and M.A. acknowledge the Sardinia Regional Government for financial support (POR Sardegna FSE Operational Programme of the Autonomous Region of Sardinia, European Social Fund 2007-2013 - Axis IV Human Resources, Objective l.3, Line of Activity l.3.1 “Avviso di chiamata per il finanziamento di Assegni di Ricerca”).

■ REFERENCES

(1) (a) *Bioinorganic Medicinal Chemistry*; Alessio, E., Ed.; Wiley-VCH: Weinheim, Germany, 2011; Topics in Organometallic Chemistry 32. (b) *Medicinal Organometallic Chemistry*, Jaouen, G., Metzler-Nolte, N., Eds.; Springer-Verlag: Berlin, Heidelberg, 2010;.

(c) *Metals in Medicine*, Dabrowiak, J. C., Ed.; Wiley: Chichester, U.K., 2009.

(2) Bergamo, A.; Gaiddon, C.; Schellens, J. H. M.; Beijnen, J. H.; Sava, G. *J. Inorg. Biochem.* **2012**, *106*, 90−99.

(3) Kaluderovic, G. N.; Paschke, R. *Curr. Med. Chem.* **2011**, *18* (31), 4738−4752.

(4) Gao, E.; Liu, C.; Zhu, M.; Lin, H.; Wu, Q.; Liu, L. *Anti-Cancer Agents Med. Chem.* **2009**, *9* (3), 356−368.

(5) (a) Pacheco, E. A.; Tiekink, E. R. T.; Whitehouse, M. W. In *Gold Chemistry, Applications and Future Directions in the Life Sciences*; Mohr, F., Ed.; Wiley-VCH: Weinheim, Germany, 2009; Chapter 6, pp 283−319. (b) Che, C.-M.; Sun, R. W. -Y. *Chem. Commun.* **2011**, *47*, 9554−9560.

(6) Tisato, F.; Marzano, C.; Porchia, M.; Pellei, M.; Santini, C. *Med. Res. Rev.* **2010**, *30* (4), 708−749.

(7) Leung, C.-H.; Zhong, H.-J.; Chan, D. S. -H.; Ma, D.-L. *Coord. Chem. Rev.* **2013**, *257*, 1764−1776.

(8) McKeage, M. J.; Maharaj, L.; Berners-Price, S. J. *Coord. Chem. Rev.* **2002**, *232*, 127−135.

(9) Tiekink, E. R. T. *Crit. Rev. Oncol. Hematol.* **2002**, *42*, 225−248.

(10) (a) Barnard, P. J.; Berners-Price, S. J. *Coord. Chem. Rev.* **2007**, *251*, 1889−1902. (b) Ott, I. *Coord. Chem. Rev.* **2009**, *253*, 1670−1681.

(11) Messori, L.; Abbate, F.; Marcon, G.; Orioli, P.; Fontani, M.; Mini, E.; Mazzei, T.; Carotti, S.; O'Connell, T.; Zanello, P. *J. Med. Chem.* **2000**, *43*, 3541−3548.

(12) (a) Marcon, G.; Carotti, S.; Coronnello, M.; Messori, L.; Mini, E.; Orioli, P.; Mazzei, T.; Cinellu, M. A.; Minghetti, G. *J. Med. Chem.* **2002**, *45*, 1672−1677. (b) Gabbiani, C.; Guerri, A.; Cinellu, M. A.; Messori, L. *Open Crystallogr. J.* **2010**, *3*, 29−40.

(13) Che, C.-M.; Sun, R. W.; Yu, W. Y.; Ko, C. B.; Zhu, N.; Sun, H. *Chem. Commun.* **2003**, *14*, 1718−1719.

(14) Ronconi, L.; Marzano, C.; Zanello, P.; Corsini, M.; Miolo, G.; Macca, C.; Trevisan, A.; Fregona, D. *J. Med. Chem.* **2006**, *49*, 1648−1657.

(15) (a) Sun, R. W. -Y.; Lok, C.-N.; Fong, T. T.-H.; Li, C. K. -L.; Yang, Z. F.; Zou, T.; Siu, A. F.-M.; Che, C.-M. *Chem. Sci.* **2013**, *4*, 1979−1988. (b) Cutillas, N.; Yellol, G. S.; de Haro, C.; Vicente, C.; Rodríguez, V.; Ruiz, J. *Coord. Chem. Rev.* **2013**, *257*, 2784−2797.

(16) (a) Nobili, S.; Mini, E.; Landini, I.; Gabbiani, C.; Casini, A.; Messori, L. *Med. Res. Rev.* **2010**, *30*, 550−580. (b) Cattaruzza, L.; Fregona, D.; Mongiat, M.; Ronconi, L.; Fassina, A.; Colombatti, A.; Aldinucci, D. *Int. J. Cancer.* **2011**, *128*, 206−215. (c) Zhang, J.-J.; Sun, R. W.-Y.; Che, C.-M. *Chem. Commun.* **2012**, *48*, 3388−3390. (d) Zhang, J.-J.; Ng, K.-M.; Lok, C.-N.; Sun, R. W.-Y.; Che, C.-M. *Chem. Commun.* **2013**, *49*, 5153−5155.

(17) (a) Zhang, X.; Frezza, M.; Milacic, V.; Ronconi, L.; Fan, Y.; Bi, C.; Fregona, D.; Dou, Q. P. *J. Cell Biochem.* **2010**, *109*, 162−172. (b) Milacic, V.; Chen, D.; Ronconi, L.; Landis-Piwowar, K. R.; Fregona, D.; Dou, Q. P. *Cancer Res.* **2006**, *66*, 10478−10486.

(18) Berners-Price, S. J.; Filipovska, A. *Metallomics* **2011**, 3, 863−873.

(19) Micale, N.; Cinellu, M. A.; Maiore, L.; Sannella, A. R.; Severini, C.; Schirmeister, T.; Gabbiani, C.; Messori, L. *J. Inorg. Biochem.* **2011**, *105*, 1576−1579.

(20) Colotti, G.; Ilari, A.; Fiorillo, A.; Baiocco, P.; Cinellu, M. A.; Maiore, L.; Scaletti, F.; Gabbiani, C.; Messori, L. *ChemMedChem* **2013**, *8*, 1634−1637.

(21) Vieites, M.; Smircich, P.; Guggeri, L.; Marchán, E.; Gómez-Barrio, A.; Navarro, M.; Garat, B.; Gambino, D. *J. Inorg. Biochem.* **2009**, *103*, 1300−1306.

(22) (a) Mphahlele, M.; Papathanasopoulos, M.; Cinellu, M. A.; Coyanis, M.; Mosebi, S.; Traut, T.; Modise, R.; Coates, J.; Hewer, R. *Bioorg. Med. Chem.* **2012**, *20*, 401−407. (b) Lewis, M.; DaFonseca, G. S.; Chomont, N.; Palamara, A. T.; Tardugno, M.; Mai, A.; Collins, M.; Wagner, W. L.; Yalley-Ogunro, J.; Greenhouse, J.; Chirullo, B.; Norelli, S.; Garaci, E.; Savarino, A. *AIDS* **2011**, *25*, 1347−1356.

(23) Niven, A. S.; Argyros, G. *Chest* **2003**, *123* (4), 1254−1265.

(24) Wang, Y.; Xu, J.; Wang, L.; Zhang, B.; Du, W. *Chem. Eur. J.* **2010**, *16*, 13339−13342.

(25) (a) Casini, A.; Cinellu, M. A.; Minghetti, G.; Gabbiani, C.; Coronnello, M.; Mini, E.; Messori, L. *J. Med. Chem.* **2006**, *49* (18), 5524−5531. (b) Cinellu, M. A.; Maiore, L.; Manassero, M.; Casini, A.; Arca, M.; Fiebig, H. H.; Kelter, G.; Michelucci, E.; Pieraccini, G.; Gabbiani, C.; Messori, L. *ACS Med. Chem. Lett.* **2010**, *1*, 336−339.

(26) Gabbiani, C.; Casini, A.; Messori, L.; Guerri, A.; Cinellu, M. A.; Minghetti, G.; Corsini, M.; Rosani, C.; Zanello, P.; Arca, M. *Inorg. Chem.* **2008**, *47*, 2368−2379.

(27) Serratrice, M.; Cinellu, M. A.; Maiore, L.; Pilo, M.; Zucca, A.; Gabbiani, C.; Guerri, A.; Landini, I.; Nobili, S.; Mini, E.; Messori, L. *Inorg. Chem.* **2012**, *51*, 3161−3171.

(28) Schiffmann, R.; Neugebauer, A.; Klein, C. D. *J. Med. Chem.* **2006**, *49*, 511−522.

(29) Tsukamoto, G.; Yoshino, K.; Kohono, T.; Ohtaka, H.; Kagaya, H.; Ito, K. *J. Med. Chem.* **1980**, *23*, 734−738.

(30) The highest cytotoxicity was found in those complexes bearing the Au^I−PPh_3 moiety, **5** and $(\mathbf{8}^+)(PF_6^-)$−$(\mathbf{10}^+)(PF_6^-)$ being the most active against the A2780/S cell line (IC_{50} 0.6 μM) and only slightly less active against the resistant line A2780/R (IC_{50} 0.9−3.3 μM).

(31) (a) Addison, A. W.; Rao, T. N.; Waslgren, C. G. *J. Heterocycl. Chem.* **1983**, *20*, 1481−1484. (b) Alcade, E.; Dinarés, I.; Pérez-Garzia, L.; Roca, T. *Synthesis* **1992**, 395−398. (c) Likhanova, N. V.; Veloz, M. A.; Höpfl, H.; Matías, D. J.; Reyes-Cruz, V. E.; Olivares, O.; Martínez-Palou, R. *J. Heterocycl. Chem.* **2007**, *44*, 145−153.

(32) Tzeng, B.-C.; Chen, B.-S.; Chen, C.-K.; Chang, Y.-P.; Tzeng, W.-C.; Lin, T. Y.; Lee, G.-H.; Chou, P. T.; Fu, Y.-J.; Chang, A. H.-H. *Inorg. Chem.* **2011**, *50*, 5379−5388.

(33) Compound $(\mathbf{10}^+)(PF_6^-)$ could be prepared also from **5** in the presence of another 1 mol of $[(Ph_3P)Au^+](PF_6^-)$.

(34) Khalil, M. M. H. *Transition Met. Chem.* **2000**, *25*, 358−360.

(35) Zhu, S.; Gorski, W.; Powell, D. R.; Walmsley, J. A. *Inorg. Chem.* **2006**, *45*, 2688−2694.

(36) Sanna, G.; Pilo, M. I.; Minghetti, G.; Cinellu, M. A.; Spano, N.; Seeber, R. *Inorg. Chim. Acta* **2000**, *310*, 34−40.

(37) The spectroscopic features of pbiH in CH_2Cl_2 closely recall those reported in 1,2-dichloroethane (DCE) and CH_3CN solutions. DCE: λ_{max} 310.5 nm (ε = 22600 M^{-1} cm^{-1}); λ_{em} 360 nm.[38] CH_3CN: λ_{max} 310.0 nm (ε = 26000 M^{-1} cm^{-1}); λ_{em} 370 nm.[39]

(38) Kondo, M. *Bull. Chem. Soc. Jpn.* **1978**, *51*, 3027.

(39) Brown, R. G.; Entwistle, N.; Hepworth, J. D.; Hodgson, K. W.; May, B. *J. Phys. Chem.* **1982**, *86*, 2418−2420.

(40) Rodriguez Prieto, F.; Mosquera, M.; Novo, M. *J. Phys. Chem.* **1990**, *94*, 8536−8542.

(41) Iyer, E. S. S.; Samanta, D.; Dey, A.; Kundu, A.; Datta, A. *J. Chem. Phys. B* **2012**, *116*, 1586−1592.

(42) Aragoni, M. C.; Arca, M.; Crisponi, G.; Nurchi, V. M. *Anal. Chim. Acta* **1995**, *316*, 195−204.

(43) (a) Becke, A. D. *J. Chem. Phys.* **1993**, *98*, 5648−5652. (b) Lee, C.; Yang, W.; Parr, R. G. *Phys. Rev. B* **1988**, *37*, 785−789. (c) Stephens, P. J.; Devlin, F. J.; Chabalowski, C. F.; Frisch, M. J. *J. Phys. Chem.* **1994**, *98*, 11623−11627.

(44) Adamo, C.; Barone, V. *J. Chem. Phys.* **1998**, *108*, 664−675.

(45) Adamo, C.; Barone, V. *J. Chem. Phys.* **1999**, *110*, 6158−6170.

(46) Gorin, D.; Toste, D. *Nature* **2007**, *446*, 395−403 and references therein.

(47) Ross, R. B.; Powers, J. M.; Atashroo, T.; Ermler, W. C.; LaJohn, L. A.; Christiansen, P. A. *J. Chem. Phys.* **1990**, *93*, 6654−6670.

(48) Roy, L. E.; Hay, P. J.; Martin, R. L. *J. Chem. Theory Comput.* **2008**, *4*, 1029−1031.

(49) (a) Binkley, J. S.; Pople, J. A.; Hehre, W. J. *J. Am. Chem. Soc.* **1980**, *102*, 939−947. (b) Stevens, W. J.; Krauss, M.; Basch, H.; Jasien, P. G. *Can. J. Chem.* **1992**, *70*, 612−630.

(50) (a) Bergner, A.; Dolg, M.; Kuechle, W.; Stoll, H.; Preuss, H. *Mol. Phys.* **1993**, *80*, 1431−1441. (b) Kaupp, M.; Schleyer, P. v. R.; Stoll, H.; Preuss, H. *J. Chem. Phys.* **1991**, *94*, 1360−1366. (c) Dolg, M.; Stoll, H.; Preuss, H.; Pitzer, R. M. *J. Phys. Chem.* **1993**, *97*, 5852−5859.

(51) (a) Jacquemin, D.; Perpète, E. A.; Scalmani, G.; Frisch, M. J.; Assfeld, X.; Ciofini, I.; Adamo, C. *J. Chem. Phys.* **2006**, *125*, 164324−1−11. (b) Jacquemin, D.; Perpete, E. A.; Scuseria, G. E.; Ciofini, I.;

Adamo, C. *J. Chem. Theory Comput.* **2008**, *4*, 123−135. (c) Pintus, A.; Aragoni, M. C.; Bellec, N.; Devillanova, F. A.; Lorcy, D.; Isaia, F.; Lippolis, V.; Randall, R. A. M.; Roisnel, T.; Slawin, A. M. Z.; Woollins, J. D.; Arca, M. *Eur. J. Inorg. Chem.* **2012**, 3577−3594. (d) Höfener, S.; Kooijman, P. C.; Groen, J.; Ariese, F.; Visscher, L. *Phys. Chem. Chem. Phys.* **2013**, *15*, 12572−12581.

(52) Tomasi, J.; Mennucci, B.; Cammi, R. *Chem. Rev.* **2005**, *105*, 2999−3094.

(53) Wiberg, K. *Tetrahedron* **1968**, *24*, 1083−1096.

(54) Forcing the molecules of pbi$^-$ in **4**$^+$ and **5** to be planar ($\tau = 0°$) results in negative vibrational frequencies.

(55) (a) Reed, A. E.; Curtiss, L. A.; Weinhold, F. *Chem. Rev.* **1988**, *88*, 899−926. (b) Carpenter, J. E.; Weinhold, F. *J. Mol. Struct (THEOCHEM)* **1988**, *169*, 41−62.

(56) For example, **4**$^+$ and **5**, which are isoelectronic and differ only in the N-protonation of the pbiH ligand, feature in the gas phase a difference in the $\varepsilon_{\mathrm{HOMO}}$ and $\varepsilon_{\mathrm{LUMO}}$ values larger than 3 eV in the gas phase and about 1.2 eV when the solvent is implicitly considered at the IEF-SCRF level.

(57) Aragoni, M. C.; Arca, M.; Demartin, F.; Devillanova, F. A.; Garau, A.; Isaia, F.; Lelj, F.; Lippolis, V.; Verani, G. *J. Am. Chem. Soc.* **1999**, *121*, 7098−7107.

(58) Accordingly, a variation of the natural charge on the AuCl moiety of only 0.031e was calculated when passing from the neutral species **3** to the hypothetical monoreduced form **3**$^-$.

(59) Cinellu, M. A.; Minghetti, G.; Cocco, F.; Stoccoro, S.; Zucca, A.; Manassero, M.; Arca, M. *Dalton Trans.* **2006**, 5703−5716.

(60) (a) Chatt, J.; Duncanson, L. A. *J. Chem. Soc.* **1953**, 23939−2947. (b) Dewar, J. S. *Bull. Chem. Soc. Fr.* **1951**, *18*, C71−C79.

(61) The simulated UV−vis absorption spectrum of the hypothesized dimer $(\mathbf{3})_2$ does not show significant differences with respect to the spectrum simulated for the monomer (calculated uncorrected maxima of the absorption wavelength 212 and 296 nm).

(62) Kasha, M. *Discuss. Faraday Soc.* **1950**, *9*, 14−19.

(63) Cassano, T.; Tommasi, R.; Nitti, L.; Aragoni, M. C.; Arca, M.; Denotti, C.; Devillanova, F. A.; Isaia, F.; Lippolis, V.; Lelj, F.; Romaniello, P. *J. Chem. Phys.* **2003**, *118*, 5995−6002.

(64) Forster, L. S. *Coord. Chem. Rev.* **2006**, *250*, 2023−2033.

(65) Cannizzo, A.; Blanco-Rodríguez, A. M.; El Nahhas, A.; Šebera, J.; Zális, S.; Vlčec, A., Jr.; Chergui, M. *J. Am. Chem. Soc.* **2008**, *130*, 8967−8974.

(66) (a) Tatchen, J.; Gilka, N.; Marian, C. M. *Phys. Chem. Chem. Phys.* **2007**, *9*, 5209−5221. (b) Chiodo, S.; Russo, N. *Chem. Phys. Lett.* **2010**, *490*, 90−96.

(67) The least-squares fitting in Figure 11 does not include complex **5**, whose data fall in the fourth quadrant, and complex **7**, considered as an anomaly. If complex **7** is included, the R^2 value is lowered to 0.83, with slope −0.261 eV^{-1} and intercept 1.636.

(68) The same linear fitting between log IC_{50} and $\varepsilon_{\mathrm{LUMO}}$ can be extended to the values determined with the A2780/S cell line: slope −0.283 eV^{-1}, intercept 1.405, $R^2 = 0.71$.

(69) McKeage, M. J.; Maharaj, L.; Berners-Price, S. J. *Coord. Chem. Rev.* **2002**, *232*, 127−135.

(70) Lakiwick, J. R. In *Principles of Fluorescence Spectroscopy*; Kluwer Academic/Plenum: New York, 1999.

(71) *Fityk 0.9*; http://www.unipress.waw.pl/fityk/.

(72) Frisch, M. J.; Trucks, G. W.; Schlegel, H. B.; Scuseria, G. E.; Robb, M. A.; Cheeseman, J. R.; Scalmani, G.; Barone, V.; Mennucci, B.; Petersson, G. A.; Nakatsuji, H.; Caricato, M.; Li, X.; Hratchian, H. P.; Izmaylov, A. F.; Bloino, J.; Zheng, G.; Sonnenberg, J. L.; Hada, M.; Ehara, M.; Toyota, K.; Fukuda, R.; Hasegawa, J.; Ishida, M.; Nakajima, T.; Honda, Y.; Kitao, O.; Nakai, H.; Vreven, T.; Montgomery, J. A., Jr.; Peralta, J. E.; Ogliaro, F.; Bearpark, M.; Heyd, J. J.; Brothers, E.; Kudin, K. N.; Staroverov, V. N.; Kobayashi, R.; Normand, J.; Raghavachari, K.; Rendell, A.; Burant, J. C.; Iyengar, S. S.; Tomasi, J.; Cossi, M.; Rega, N.; Millam, N. J.; Klene, M.; Knox, J. E.; Cross, J. B.; Bakken, V.; Adamo, C.; Jaramillo, J.; Gomperts, R.; Stratmann, R. E.; Yazyev, O.; Austin, A. J.; Cammi, R.; Pomelli, C.; Ochterski, J. W.; Martin, R. L.; Morokuma, K.; Zakrzewski, V. G.; Voth, G. A.; Salvador, P.; Dannenberg, J. J.; Dapprich, S.; Daniels, A. D.; Farkas, Ö.; Foresman, J. B.; Ortiz, J. V.; Cioslowski, J.; Fox, D. J. *Gaussian 09, Revision A.02*; Gaussian, Inc., Wallingford, CT, 2009.

(73) Frisch, Æ.; Frisch, M. J. *GAUSSIAN09 User's Reference*; Gaussian, Inc.: Pittsburgh, PA, 1998, and references therein.

(74) Schäfer, A.; Horn, H.; Ahlrichs, R. *J. Chem. Phys.* **1992**, *97*, 2571−2577.

(75) (a) Feller, D. *J. Comput. Chem.* **1996**, *17*, 1571−1586. (b) Schuchardt, K. L.; Didier, B. T.; Elsethagen, T.; Sun, L.; Gurumoorthi, V.; Chase, J.; Li, J.; Windus, T. L. *J. Chem. Inf. Model* **2007**, *47*, 1045−1052.

(76) Schaftenaar, G.; Noordik, J. H. *J. Comput.-Aided Mol. Design* **2000**, *14*, 123−134.